



ELSEVIER

Pattern Recognition Letters 20 (1999) 383–393

Pattern Recognition  
Letters

# Dynamic motion analysis using wavelet flow surface images

Jae-Khun Chang<sup>1</sup>, Terry L. Huntsberger<sup>\*,2</sup>

*Department of Computer Science, Intelligent Systems Laboratory, University of South Carolina, Columbia, SC 29208, USA*

Received 12 September 1996; received in revised form 8 November 1998

## Abstract

We have developed a motion analysis method that combines the wavelet transform with the flow surface image technique. In dynamic navigation environments, whenever objects move, the projections of the objects onto the image plane also move. These projections build over time spatiotemporal surfaces of their movement and volumes created by the surfaces. This paper presents a new method for the interpretation of optical flow for moving objects from a sequence of images. Flow surface images of the moving objects are created within the wavelet-derived space, chosen from seven different directionally sensitive detail images using the 3D wavelet decomposition. The motion estimation algorithm concentrates on the integration of information from the flow surface images, followed by a quadratic patch parameterization and determination of flow paths of the end points of edges on the flow surface images. The results of two experimental studies with an object exhibiting out-of-plane translation and rotation are also reported. © 1999 Elsevier Science B.V. All rights reserved.

**Keywords:** Flow surface; Optical flow; Wavelets; Patch parameterization

## 1. Introduction

An important goal of computer vision is the analysis of the motion characteristics of the observer and the objects in dynamic scenes for the recovery of 3D surface information. There are three approaches that can be used to interpret the motion of objects: gradient approach, correspon-

dence approach, and spatiotemporal method. Good reviews can be found in (Aggarwal and Nandhakumar, 1988; Barron et al., 1994; Beauchemin and Barron, 1995). An approach which uses a fusion of results from all three methods was developed by Singh (1991).

The gradient approach is based on the computation of image changes in space and time (e.g. Horn and Schunck, 1981; Snyder, 1991). The gradient method does not allow for acceleration in the optic flow calculation and is sensitive to noise in the gradients. In addition, the brightness constancy assumption is violated by light source motion and/or shadows. The method has recently been extended by Negahdaripour (1998) to include variations in lighting by decoupling geometric and radiometric sources of scene gradients. Similar studies along these lines can be found in (Cornelius

\* Corresponding author. Tel.: 803 777 2404; fax: 803 777 3767; e-mail: terry@cs.sc.edu

<sup>1</sup> Now with the Department of Computer Science, Hanshin University, Kyung-Ki Do Osan City, Yang-san Dong 411, S. Korea, 447-791.

<sup>2</sup> Research supported in part under ONR Grant no. N00014-94-1-1163. Reprints of this paper can be obtained by contacting the author at terry@cs.sc.edu. The authors would like to thank the reviewers whose comments have led to a more readable manuscript.

and Kanade, 1983; Schunck, 1985; Nagel, 1989; Verri and Poggio, 1989). A recent experimental study by Brandt (1997) indicated that small-support low-pass prefiltering of the input sequence led to better accuracy in the optic flow computation.

In the correspondence method, points, lines, or regions of objects in the first image are put into correspondence with similar features later in the sequence (e.g. Huntsberger and Jayaramamurthy, 1987; Liu and Huang, 1986; Roach and Aggarwal, 1980). A study by Weng et al. (1993) indicated that even small errors of one or two pixels in image coordinates used for point correspondence cause an ambiguous interpretation of translation or rotation due to violation of the epipolar constraint. Their solution was to use a two-step approach that consisted of a linear solution of the closed-form correspondence equations, followed by a minimization of image errors using a minimum variance estimator technique. A recent analysis by Zhang (1995) demonstrated that 3D motion and structure parameters can be derived from corresponding line segments in just two perspective images. His study uses an epipolar (EPI) geometry constraint on the common part of the corresponding line segments.

Another approach for motion analysis and the method used in our study is to consider a 3D spatiotemporal image (e.g. Allmen and Dyer, 1991; Baker and Bolles, 1989; Rangachar et al., 1990), where a temporal cube is built by stacking together a sequence of images. Work also related to this approach is the spatiotemporal filters of Fleet and Jepson (1990) and Heeger (1988), where a frequency space analysis is performed using tuned filters. A recent study by Otsuka et al. (1997) used a 3D Hough transform for planar surface detection to derive spatiotemporal surfaces (trajectory surfaces). Although robust, the method suffers from a high computational cost from the Hough transform. We use a local region growing approach followed by a Monge patch parameterization to derive the spatiotemporal surfaces in the wavelet coefficient spaces.

In general, 3D motion analysis computes the motion and structure of objects from a sequence of images using two steps. The first step is to compute observables (features or optical flow) in the im-

ages; followed by the extraction of the motion and structure of objects using the observables. Closed form solutions for derivation of the structure and motion parameters have been developed by Subbarao (1989) and Waxman et al. (1987). This paper uses a combination of feature extraction and optical flow derived from the flow surface of wavelet-derived edge points in a sequence of images for the first motion analysis step. In a further study, Chang (1997) used the solution of a linear set of equations derived from the optical flow of the surfaces to derive the structure and motion parameters of the objects.

Huntsberger et al. (1994) focused on wavelet-derived epipolar-plane image (EPI) analysis, and alleviated some of the problems in the interpretation of translation in depth and occlusion/disocclusion. Allmen and Dyer (1990, 1991) have studied the spatiotemporal surface flow method for motion estimation. They assumed that the arc length of a segment is constant throughout the temporal slices. Although this assumption is applied to vertical and horizontal movement, out-of-plane translation would be problematic. Chang and Huntsberger (1996) in their study of a wavelet flow surface motion analysis method created spatiotemporal surfaces for pure translation and pure rotation of simple lines. The partial derivatives from the patch parameterization of the flow surface were then used to derive the optical flow. The wavelet method has an advantage over that of Allmen and Dyer (1990) in that directional information is automatically supplied by the wavelet channels, which leads to a reduction in the amount of computational processing.

In this paper, we present a new approach for the derivation of optical flow using wavelet flow surface images. This approach does not require texture for differentiation or correlation, but only uses spatiotemporal flow surfaces. The new method applies factors for noise reduction, feature grouping, and surface smoothness. Using the directional sensitivity of wavelet-derived coefficients, the computational speed is faster than the previous methods. The slope of the wavelet-derived flow surfaces are computed to determine optic flow for out-of-plane translation and rotation of a rigid object.

Section 2 contains a brief review of wavelet decomposition and characteristics of 3D wavelet coefficients. This is followed by a discussion of the flow surface method for the extraction of the optical flow. The final section gives the results of some experimental studies of a object undergoing out-of-plane translation and rotation in an industrial environment.

## 2. Wavelet analysis

Grossmann and Morlet (1984) developed the continuous wavelet representation for one-dimensional signals to analyze seismic data. The wavelet functions were constructed as continuous translations and dilations of one function with local support in time and frequency domain. The wavelet representation has good localization properties in the frequency and spatial domains. Another benefit of the wavelet representation is that the filters used are orientation sensitive. The horizontal, vertical, or even temporal orientation sensitivities of the orthogonal wavelet decomposition exhibit good advantages for motion detection in a sequence of images.

The standard wavelet decomposition of a general signal  $f \in L^2(\mathbf{R})$  is a representation in terms of linear combinations of translated dilates of a single function  $\psi$ :

$$f(x) = \sum_{j,k=-\infty}^{\infty} c_{j,k} \psi_{j,k}(x), \quad (1)$$

where  $\psi_{j,k}(x) = 2^{j/2} \psi(2^j x - k)$  and the coefficients  $c_{j,k}$  are called the wavelet coefficients for integer  $j$  and  $k$ . The projection  $P_j f(x)$  is an approximation of  $f(x)$  at resolution  $2^j$ , that is,

$$P_j f(x) = v_j(x) = \sum_k v_{j,k} \phi_{j,k}(x), \quad (2)$$

where  $v_{j,k} = \langle f(x), \phi_{j,k}(x) \rangle$  and  $\phi_{j,k}(x) = 2^{j/2} \phi(2^j x - k)$ . In the vector space  $V_j$  that forms an orthonormal basis and satisfies the property  $V_j \subset V_{j+1}$ ,  $W_{j-1}$  is an element of the orthogonal complement of  $V_{j-1}$  in  $V_j$ . A general overview of wavelet analysis can be found in (Daubechies, 1992; Chui, 1992; Mallat, 1998).

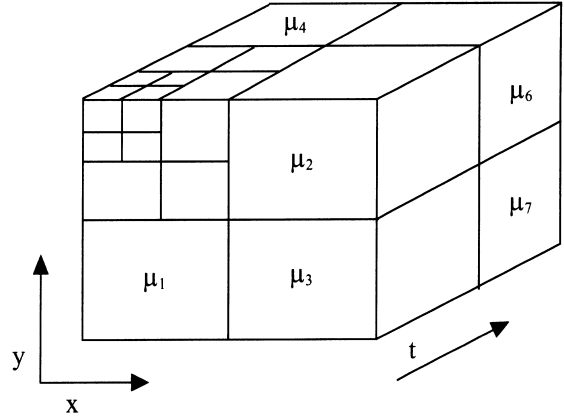


Fig. 1. 3D wavelet decomposition and multiresolution structure of image sequence.

In order to apply wavelet decompositions to multi-dimensional signals, the multi-dimensional extensions of wavelets are required. An obvious way is to use separate wavelets obtained from the products of one-dimensional wavelets and scaling functions as in (Mallat, 1989). By carrying out a one-dimensional wavelet decomposition for each variable  $(x, y, t)$  separately, we obtain

$$f(x, y, t) = \sum_{k_1, k_2, k_3} v_{j,k_1,k_2,k_3} \phi_{j,k_1}(x) \phi_{j,k_2}(y) \phi_{i,k_3}(t). \quad (3)$$

Note that in the 3D wavelet decomposition, we apply the 2D wavelet decomposition to each image and then apply a one-dimensional transform to the sequence of images, time dimension  $t$ . We have seven 3D wavelet coefficients,  $\mu_i$  ( $i = 1, 7$ ), shown in Fig. 1. Every 3D wavelet coefficient, however, is not needed to make flow surfaces. Since the coefficients  $\mu_5$  (hidden in Fig. 1) and  $\mu_6$  are sensitive for  $y$  and  $t$  direction frequencies and  $x$  and  $t$  direction frequencies respectively, they are used for the flow surface analysis. This wavelet analysis, in which the directional information of the moving objects is derived from the wavelet filters, reduces the amount of information that is processed. Thus, the processing time of flow surface analysis in the next step is reduced as well.

## 3. Flow surface analysis

Spatiotemporal (ST) flow surfaces are the natural extension of optical flow to ST surfaces. The

structure of volumetric flow surfaces has a great deal of information about contours in a scene and their motion. Whenever objects move in the real world, the projections of the objects onto the image plane also move. These projections build, over time, ST surfaces of their movement and volumes created by the surfaces. Therefore, the motion of the objects is represented by these surfaces and volumes. For every point on an ST surface, a vector indicates the motion of that point in space–time. This vector represents the motion of points or flow. The flows of all points of an object construct surfaces in the ST volume. Allmen and Dyer (1991) introduced the ST surface flow as a flow at a point on an ST surface, and the ST flow curve as an ST curve through an ST cube such that the tangent at a point on the curve equals the ST surface flow at that point. To build an ST surface flow, they hypothesized that the arc length in a temporal slice must result in no change of arc length in the next temporal slice (Allmen and Dyer, 1990). This hypothesis has limitations in the case of out-of-plane translation or rotation.

Intensity discontinuities in each image in the sequence will show up as non-zero wavelet coefficients in the various detail channels shown in Fig. 1. These non-zero coefficients can be grouped together to build flow surfaces through the ST cube. In our flow surface analysis, we use three filter factors for building flow surface images from the wavelet derived data. These are:

1. Threshold factor ( $\alpha$ ): Used for noise reduction. The wavelet coefficients whose values are less than  $\alpha$  are removed.
2. Clustering factor ( $\beta$ ): Merges two features into one group if the difference between two features is less than  $\beta$ .
3. Smoothing factor ( $\gamma$ ): Makes the flow surface smoother by filling in small holes whose length is less than  $\gamma$  in the same group.

These three factors insure that a well-connected set of ST points are generated that are relatively smooth and free of noise.

With the filtered wavelet-derived feature data, we compute the direction in the tangent plane of the point using Monge patch parameterization of

ST surfaces. In the Monge patch parameterization, a surface can be represented as a simple form (see Besl and Jain, 1986):

$$\mathbf{x}(u, v) = (u, v, f(u, v)). \quad (4)$$

For each point in an ST volume, a quadratic patch is fit using that point and the temporal and spatial neighboring feature points to compute shape-description properties of surfaces such as partial derivatives and curvature. This quadratic patch defines  $f$ . Once the quadratic patch is fit, the partial derivatives at a point can be recovered. The partial derivatives of the surface are equal to

$$\mathbf{x}_u = (1, 0, f_u), \quad \mathbf{x}_v = (0, 1, f_v). \quad (5)$$

Since the flow surfaces are constructed using wavelet-derived feature points which are obtained from the 3D wavelet decomposition, and 3D wavelet coefficients have different responses for each 3D directional frequency, the alignment of  $u$  in Eq. (4) can be a different direction depending on the choice of 3D wavelet coefficients. The time direction always lies along the  $v$  axis for patch parameterization. The edges of the flow surfaces correspond to feature endpoints in the original images. We assume polyhedral objects in our analysis, meaning that these points are indicative of corners of the objects. The optic flow is derived from these points in order to address the aperture problem for other points in the interior area of the flow surfaces.

One clear way to derive the partial derivatives of the surface when referring to patch parameterization is to assume that in each neighborhood of the parameter plane, the underlying quadratic patch function  $f$  takes the parametric form of a polynomial in the spatial and temporal coordinates, and that the sampling producing the parameter plane is a regular equal interval grid sampling of the plane which is the domain of  $f$ . Therefore, in each neighborhood  $f$  has this polynomial form:

$$f(u, v) = a_0 + a_1u + a_2v + a_3u^2 + a_4uv + a_5v^2 + a_6u^3 + a_7u^2v + a_8uv^2 + a_9v^3. \quad (6)$$

From Eqs. (5) and (6), the partial derivatives of every point on the surface can be obtained from

1/9	<table><tr><td>1</td><td>1</td><td>1</td></tr><tr><td>1</td><td>1</td><td>1</td></tr><tr><td>1</td><td>1</td><td>1</td></tr></table>	1	1	1	1	1	1	1	1	1	1/6	<table><tr><td>-1</td><td>0</td><td>1</td></tr><tr><td>-1</td><td>0</td><td>1</td></tr><tr><td>-1</td><td>0</td><td>1</td></tr></table>	-1	0	1	-1	0	1	-1	0	1	1/6	<table><tr><td>1</td><td>1</td><td>1</td></tr><tr><td>0</td><td>0</td><td>0</td></tr><tr><td>-1</td><td>-1</td><td>-1</td></tr></table>	1	1	1	0	0	0	-1	-1	-1
1	1	1																														
1	1	1																														
1	1	1																														
-1	0	1																														
-1	0	1																														
-1	0	1																														
1	1	1																														
0	0	0																														
-1	-1	-1																														
1/6	<table><tr><td>1</td><td>-2</td><td>1</td></tr><tr><td>1</td><td>-2</td><td>1</td></tr><tr><td>1</td><td>-2</td><td>1</td></tr></table>	1	-2	1	1	-2	1	1	-2	1	1/4	<table><tr><td>-1</td><td>0</td><td>1</td></tr><tr><td>0</td><td>0</td><td>0</td></tr><tr><td>1</td><td>0</td><td>-1</td></tr></table>	-1	0	1	0	0	0	1	0	-1	1/6	<table><tr><td>1</td><td>1</td><td>1</td></tr><tr><td>-2</td><td>-2</td><td>-2</td></tr><tr><td>1</td><td>1</td><td>1</td></tr></table>	1	1	1	-2	-2	-2	1	1	1
1	-2	1																														
1	-2	1																														
1	-2	1																														
-1	0	1																														
0	0	0																														
1	0	-1																														
1	1	1																														
-2	-2	-2																														
1	1	1																														
1/4	<table><tr><td>1</td><td>-2</td><td>1</td></tr><tr><td>0</td><td>0</td><td>0</td></tr><tr><td>-1</td><td>2</td><td>-1</td></tr></table>	1	-2	1	0	0	0	-1	2	-1	1/4	<table><tr><td>-1</td><td>0</td><td>1</td></tr><tr><td>2</td><td>0</td><td>-2</td></tr><tr><td>-1</td><td>0</td><td>1</td></tr></table>	-1	0	1	2	0	-2	-1	0	1	1/4	<table><tr><td>1</td><td>-2</td><td>1</td></tr><tr><td>-2</td><td>4</td><td>-2</td></tr><tr><td>1</td><td>-2</td><td>1</td></tr></table>	1	-2	1	-2	4	-2	1	-2	1
1	-2	1																														
0	0	0																														
-1	2	-1																														
-1	0	1																														
2	0	-2																														
-1	0	1																														
1	-2	1																														
-2	4	-2																														
1	-2	1																														

Fig. 2. Nine coefficient filters used for discretized quadratic polynomial approximation of flow surface.

$$f_u = a_1, \quad f_v = a_2. \quad (7)$$

A polynomial basis set which permits the independent estimation of each coefficient is used to estimate the coefficients of the linear combinations.

The coefficient estimates for fitting are calculated as linear combinations of the sampled data values using a procedure given by Forsythe (1957):

$$f(x) = \sum_{i=0}^{n-1} k_i p_i(x). \quad (8)$$

In 1D, this process minimizes the sum of the squared differences between the actual data values and a polynomial series approximation:

$$E^2 = \sum_{x \in S} \left[ f(x) - \sum_{i=0}^j k_i p_i(x) \right]^2. \quad (9)$$

where  $S$  is the index set for the polynomial. Solving for  $k_i$  gives

$$k_i = \frac{\sum_{x \in S} p_i(x) f(x)}{\sum_{x \in S} p_i^2(x)}. \quad (10)$$

These coefficients for the  $3 \times 3$  index set used in our surface building process are derived in a study by Haralick (1984) and are shown in Fig. 2.

#### 4. Experimental study

We performed three experimental studies to test our method. The first used a box moving with out-of-plane translation (in depth), and the second and third used a box moving with two different rates of out-of-plane rotation. The box is manually moved for each frame in the sequence which gives us the exact flow since we use calibration marks on the floor to measure distances. Our previous studies using generated sequences of in-plane translating and rotating objects returned errors of less than 4% for the velocity values (Chang, 1997). The sequence of data used in the studies reported here had 64 frames and the image resolution was  $128 \times 128$  with 256 levels of gray. We use the corner points of the box as returned from the edges of the flow surfaces in order to eliminate possible artifacts caused by the aperture effect.

Eight sample frames from the 64 frame sequence for the first study are shown in Fig. 3, corresponding to frames 1, 10, 19, 28, 37, 46, 55 and 64. The moving object in the image sequence is the rectangular box, which follows a horizontal/depth translation path throughout the sequence.

The 3D wavelet transform was performed on the 3D spatiotemporal cube by taking the 2D transform of each image in the 64 frame sequence using Daubechies' W6 wavelet (Daubechies, 1991), followed by a 1D transform in the time direction using the same wavelet basis. Among the seven 3D wavelet-derived coefficients, two coefficients ( $\mu_5$  and  $\mu_6$ ) were taken to build flow surface images (see Fig. 1). The coefficient  $\mu_5$  has a high response for  $y$  and  $t$  directional frequencies; while  $\mu_6$  has a high response for  $x$  and  $t$  directional frequencies. Thus,  $\mu_5$  is sensitive for moving edges parallel to the  $x$ -axis; while  $\mu_6$  for moving edges parallel to the  $y$ -axis. The outline of the moving object in the sequence is shown in Fig. 4 with corner points numbered for future reference. A comparison of Figs. 1 and 4 indicates that the 3D wavelet fused data for edges 1–3 and 5–6 is well represented in  $\mu_5$ , and the 3D wavelet fused data for edges 1–2 and 4–5 is in  $\mu_6$ .

The threshold factor  $\alpha$  was chosen using the histogram of the 3D wavelet fused data. The clustering factor  $\beta$  and smoothing factor  $\gamma$  were

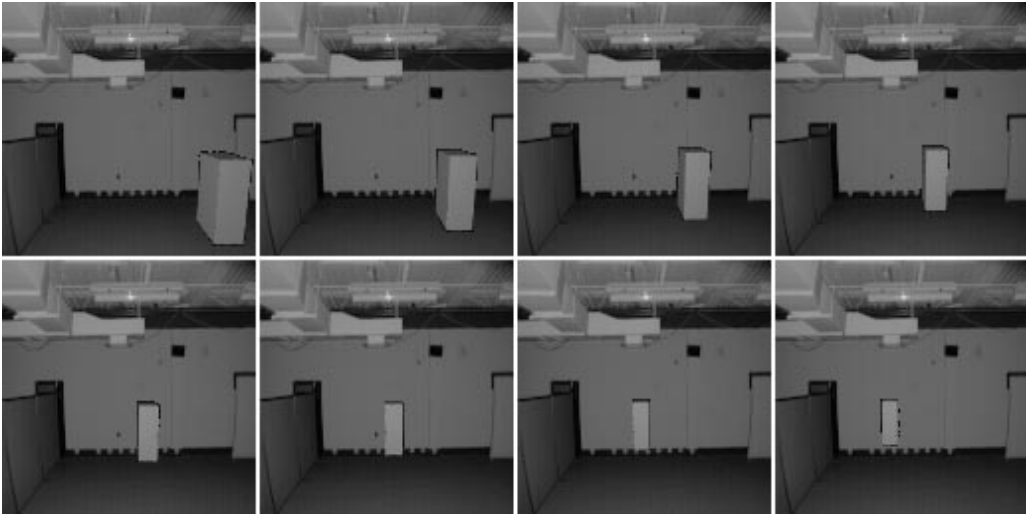


Fig. 3. 8 sample frames from the 64 frame sequence used in the first experimental study. The images have a spatial resolution of  $128 \times 128$  and a grayscale resolution of 256 levels.

determined interactively. Fig. 5 shows the patch parameterized wavelet flow surfaces of edges in Fig. 4. Time flows out of the page, and the horizontal axis is in the  $x$  direction in the upper two images in the figure, and in the  $y$  direction in the lower two images.  $\beta$  and  $\gamma$  were set to 5 for all of the edges, and  $\alpha$  was set to 2 for the upper two images and 11 for the lower two images. The threshold  $\alpha$  was different for the horizontal and vertical edges due to the strong vertical edges of the surrounding environment. The flow surface

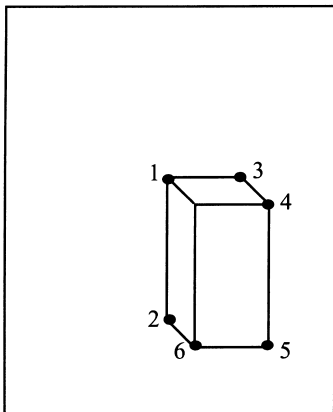


Fig. 4. Corner labels for the moving object in the first experimental sequence.

images of edges 5–6 and 4–5 become disconnected at the end of the sequence due to the small size of the moving object and noise from the back wall near the object.

The optic flow derived using the flow surface method described in the previous sections is shown in Fig. 6, where the tip of each flow vector is indicated by a bright dot. For purposes of clarity, only a sampled representation is shown. In the actual computation, the optical flow at every point of the flow surface is calculated. As was noted in the previous discussion, we only use the end points of the segments for the computation of optic flow in order to address the aperture effect. Since the polynomial fit to the flow surface was quadratic, a minimum of three images are needed for each point on the surface.

The result of the application of the flow surface analysis for the image sequence in Fig. 3 is shown in Table 1. The optical flow velocities,  $v_x$  and  $v_y$ , were computed directly from the partial derivatives and the slopes of the flow surfaces. The measured velocities of end points of each edge in Fig. 4 are given from each edge flow surface, along with the actual values from the laboratory, and the RMS error between the two. The measured velocities are taken as the average over the 64 frame sequence. All velocities are in arbitrary time units

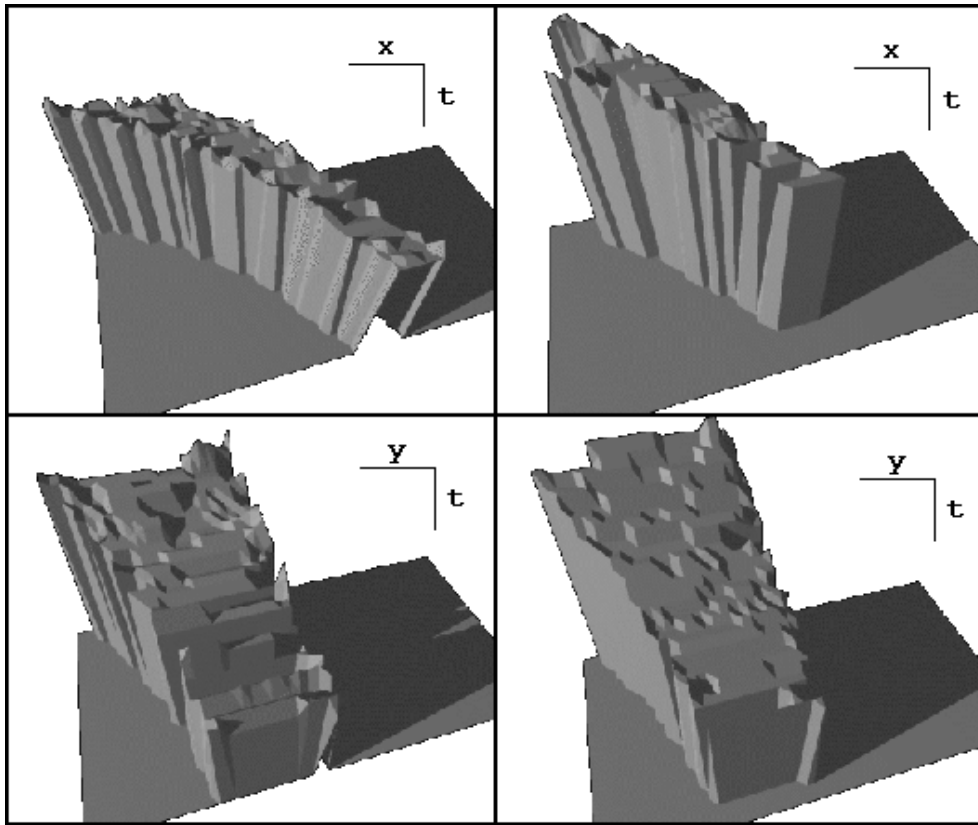


Fig. 5. Flow surface images of edges in Fig. 3; upper left: edge 1–3 using wavelet coefficient  $\mu_5$ ; upper right: edge 5–6 using wavelet coefficient  $\mu_5$ ; lower left: edge 1–2 using wavelet coefficient  $\mu_6$ ; lower right: edge 4–5 using wavelet coefficient  $\mu_6$ .

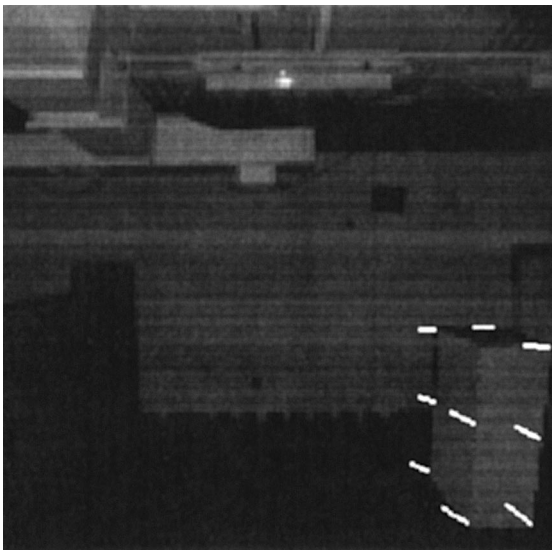


Fig. 6. Optical flow vector for out-of-plane translation in Fig. 3.

due to the single frame acquisition method employed during the experiment.

A portion of the RMS errors in Table 1 can be attributed to places in the sequence where discontinuities of the surfaces occurred, which appear as breaks in the flow surfaces shown in Fig. 5. Specifically, points 5 and 6 are very noisy in the last part of the image sequence due to the background wall. Despite this limitation, the RMS error for this approach was around 0.1 for every object point in Fig. 4.

In the second and third experimental studies, the box was rotated in place about the  $y$ -axis by a fixed number of degrees for each frame. Rotation about the  $y$ -axis gives rise to an out-of-plane rotation. Eight sample frames from the 64 frame sequence are shown in Fig. 7. We performed the two studies using rotation angles of  $3^\circ$  and  $5^\circ$ ,

Table 1

Experimental results for optical flow from 6 points on the object

Object points	Measured velocities		Actual velocities		Error
	$v_x$	$v_y$	$v_x$	$v_y$	
1	-0.788	-0.011	-0.734	-0.062	0.074
2	-0.788	-0.208	-0.734	-0.265	0.078
3	-1.000	-0.023	-0.970	-0.062	0.049
4	-1.140	-0.091	-1.080	-0.124	0.068
5	-1.178	-0.514	-1.080	-0.500	0.099
6	-1.074	-0.514	-1.000	-0.500	0.075

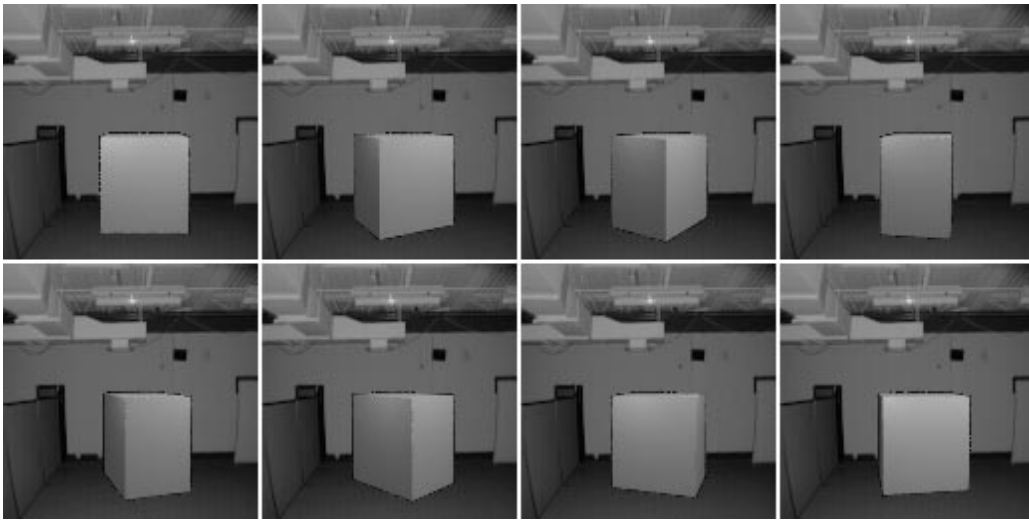


Fig. 7. 8 sample frames from the 64 frame sequence used in the second experimental study. The images have a spatial resolution of  $128 \times 128$  and a grayscale resolution of 256 levels.

respectively. The outline of the rotating object in the sequence is shown in Fig. 8 with corner points numbered for future reference. In this case new corner points appear as the sequence progresses, since sides of the box that are initially self-occluded will reappear.

For the second and third experiments the threshold factor  $\alpha$  was chosen using the histogram of the 3D wavelet fused data, and the clustering factor  $\beta$  and smoothing factor  $\gamma$  were determined interactively. Fig. 9 shows the patch parameterized wavelet flow surfaces of edges in Fig. 7. Time flows into the page, and the vertical axis is in the  $y$  direction in the upper two and lower left images in the figure, and in the  $x$  direction in the lower right image.  $\beta$  was set to 4 and  $\gamma$  was set to 5 for all of

the edges, and  $\alpha$  was set to 3 for the upper two and lower left images and 2 for the lower right image. In this case, the threshold  $\alpha$  was very close for the horizontal and vertical edges due since the box stayed in the same physical location and stray edges from the environment were not as much a problem.

The optic flow derived using the flow surface method described in the previous sections is shown in Fig. 10, where the tip of each flow vector is indicated by a bright dot. Using the derived flow vectors and the closed form solution of Subbarao and Waxman (1985) for the recovery of the surface rotation parameters gives a rotation of  $3.69^\circ/\text{frame}$  for the second experiment and  $5.14^\circ/\text{frame}$  for the third experiment or equivalent errors of 23% and



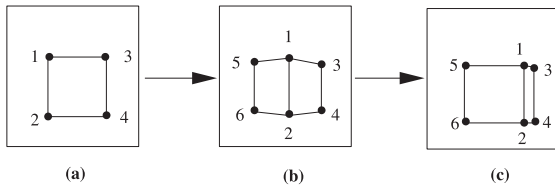


Fig. 8. Corner labels for the rotating object in the second and third experimental sequences. Note that new corner points appear as the sequence progresses.

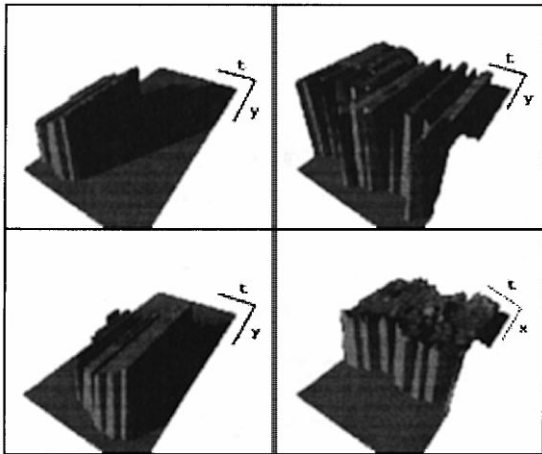


Fig. 9. Flow surface images of edges in Fig. 7; upper left: edge 1–2 using wavelet coefficient  $\mu_5$ ; upper right: edge 3–4 using wavelet coefficient  $\mu_5$ ; lower left: edge 5–6 using wavelet coefficient  $\mu_5$ ; lower right: edge 1–3 using wavelet coefficient  $\mu_3$ .

2.8%, respectively. Our previous studies (Huntsberger, 1992) into out-of-plane rotation indicated that accurate recovery of rotations less than  $4^\circ$  was not possible with the image resolution used in these two experimental studies, which may in part explain the large experimental error found in the second experiment.

## 5. Conclusions

We have presented a new method of motion analysis that combines the 3-D wavelet decomposition of an image sequence with a flow surface image analysis of the wavelet-derived volume data. The combination of patch parameterization and surface filtering for the partial derivatives was



Fig. 10. Optical flow vector for out-of-plane rotation in Fig. 7.

introduced for velocity field determination. Three factors were used to remove spurious coefficients, and to automatically smooth and cluster points for derivation of the flow surfaces. These factors resulted in better flow surface images than those of the previous method described in (Chang and Huntsberger, 1996).

This new method gives a reasonable optical flow field for out-of-plane translation in a real world image sequence, with RMS errors less than 10% in the derived optical flow velocities. In the experimental studies into out-of-plane rotation, the errors were dependent on the amount of rotation, being less than 3% for a  $5^\circ$  rotation per frame as opposed to a 23% error for a  $3^\circ$  rotation per frame. Recovery of small translation and rotation parameters is not accurate with our method due to the loss of resolution as the wavelet hierarchy is traversed. We are currently investigating the application of the method using a temporal multi-scale approach such as that used in the study done by Yacoob and Davis (1997).

## References

- Aggarwal, J.K., Nandhakumar, N., 1988. On the computation of motion from sequences of images – A review. *Proceedings of the IEEE* 76, 917–935.

- Allmen, M., Dyer, C., 1990. Computing spatiotemporal surface flow. In: Proc. 3rd Internat. Conf. Comput. Vision, pp. 47–50.
- Allmen, M., Dyer, C., 1991. Long-range spatiotemporal motion understanding using spatiotemporal flow curves. In: Proc. of the IEEE CVPR, Lahaina, Maui, Hawaii, pp. 303–309.
- Baker, H., Bolles, R., 1989. Generating epipolar-plane image analysis on the spatiotemporal surface. *Internat. J. Comput. Vision* 3, 33–49.
- Barron, J.L., Fleet, D.J., Beauchemin, S.S., 1994. Performance of optical flow techniques. *Internat. J. Comput. Vision* 12 (1), 43–77.
- Beauchemin, S.S., Barron, J.L., 1995. The computation of optical flow. *ACM Computing Surveys* 27 (3), 433–467.
- Besl, P., Jain, R., 1986. Invariant surface characteristics for 3D object recognition in range images. *CVGIP* 33, 33–80.
- Brandt, J.W., 1997. Improved accuracy in gradient-based optical flow estimation. *Internat. J. Comput. Vision* 25 (1), 5–22.
- Chang, J., 1997. Motion and structure from optical flow using wavelets and flow surface images. Ph.D. Dissertation, Department of Computer Science, U. of South Carolina.
- Chang, J., Huntsberger, T.L., 1996. Determination of the optical flow using wavelets and flow surface images. TR 9603, Department of Computer Science, U. of South Carolina.
- Chui, C.K., 1992. *An Introduction to Wavelets*. Academic Press, New York, NY.
- Cornelius, N., Kanade, T., 1983. Adapting optical flow to measure object motion in reflectance and X-ray image sequences. In: Proceedings of the ACM SIGGRAPH/SIGART Interdisciplinary Workshop on Motion: Representation and Perception, Toronto, Canada.
- Daubechies, I., 1992. *Ten Lectures on Wavelets*. CBMS 61, SIAM Press.
- Fleet, D.J., Jepson, A.D., 1990. Computation of component image velocity from local phase information. *Internat. J. Comput. Vision* 5 (1), 77–104.
- Forsythe, G.E., 1957. Generation and use of orthogonal polynomials for data-fitting with a digital computer. *J. SIAM* 5 (2), 74–88.
- Grossmann, A., Morlet, J., 1984. Decomposition of Hardy functions into square integrable wavelets of constant shape. *SIAM J. Math.* 15, 723–736.
- Haralick, R., 1984. Digital step edges from zero crossing of second directional derivative. *IEEE Trans. PAMI* 6 (1), 56–68.
- Heeger, D.J., 1988. Optical flow using spatiotemporal filters. *Internat. J. Comput. Vision* 1, 279–302.
- Horn, B., Schunck, B., 1981. Determining optical flow. *Artificial Intell.* 17, 185–203.
- Huntsberger, T.L., 1992. Data Fusion: A Neural Networks Implementation. Chapter in: Abidi, M.A., Gonzalez, R.C. (Eds.), *Data Fusion in Robotics and Machine Intelligence*. Academic Press, Orlando, FLA.
- Huntsberger, T.L., Jayaramamurthy, S., 1987. Determination of the optic flow field using the spatiotemporal deformation of region properties. *Pattern Recognition Letters* 6, 169–177.
- Huntsberger, T.L., Chang, J., Jawerth, B., 1994. Wavelet analysis of fused EPI sequences. In: Proc. SPIE Sympos. Sensor Fusion VII 2355, Boston, MA, pp. 157–163.
- Liu, Y., Huang, T., 1986. Estimation of rigid body motion using straight line correspondences. In: Proc. Workshop on Motion: Representation and Analysis, Kiawah Island, SC, pp. 47–51.
- Mallat, S., 1989. A theory for multiresolution signal decomposition: The wavelet representation. *IEEE Trans. PAMI* 11 (7), 674–693.
- Mallat, S., 1998. *A Wavelet Tour of Signal Processing*. Academic Press, New York, NY.
- Nagel, H.H., 1989. On a constraint equation for the estimation of displacement rates in image sequences. *IEEE Trans. PAMI* 11 (1).
- Negahdaripour, S., 1998. Revised definition of optical flow: Integration of radiometric and geometric cues for dynamic scene analysis. *IEEE Trans. PAMI* 20 (9), 961–979.
- Otsuka, K., Horikoshi, T., Suzuki, S., 1997. Image velocity estimation from trajectory surface in spatiotemporal space. Proceedings of IEEE CVPR, Puerto Rico, pp. 200–205.
- Rangachar, R., Hong, T.H., Herman, M., Luck, R., 1990. Analysis of optical flow estimation using epipolar plane images. In: Proceedings of SPIE Symposium on Intelligent Robots and Comp. Vision IX: Neural, Biological, and 3-D Methods 1382, Boston, MA, pp. 7–9.
- Roach, J., Aggarwal, J., 1980. Determining the movement of objects from a sequence of images. *IEEE Trans. PAMI* 2 (6), 554–561.
- Schunck, B.G., 1985. Image flow: Fundamentals and future research. In: Proceedings IEEE CVPR, San Francisco, CA.
- Singh, A., 1991. *Optic Flow Computation: A Unified Perspective*. IEEE Computer Society, Los Alamitos, CA.
- Snyder, M.A., 1991. On the mathematical foundations of smoothness constraints for the determination of optical flow and for surface reconstruction. *IEEE Trans. PAMI* 13 (11), 1105–1114.
- Subbarao, M., 1989. Interpretation of image flow: A spatiotemporal approach. *IEEE Trans. PAMI* 11 (3), 266–278.
- Subbarao, M., Waxman, A., 1985. On the uniqueness of image flow solutions for planar surfaces in motion. In: Proceedings of Third IEEE Workshop on Computer Vision: Representation and Control, Bellaire, MI, pp. 129–139.
- Verri, A., Poggio, T., 1989. Motion field and optical flow: Qualitative properties. *IEEE Trans. PAMI* 11 (5), 490–498.
- Waxman, A.M., Kamgar-Parsi, B., Subbarao, M., 1987. Closed-form solutions to image flow equations. *Internat. J. Comput. Vision* 1 (3), 12–24.
- Weng, J., Ahuja, N., Huang, T.S., 1993. Optimal motion and structure estimation. *IEEE Trans. PAMI* 15 (9), 864–884.

Yacoob, Y., Davis, L.S., 1997. Temporal multi-scale models for flow and acceleration. In: Proceedings IEEE Conf. CVPR, Puerto Rico, pp. 921–927.

Zhang, Z., 1995. Estimating motion and structure from correspondences of line segments between two perspective images. IEEE Trans. PAMI 17 (12), 1129–1139.